Research Square

Preprints are preliminary reports that have not undergone peer review.
They should not be considered conclusive, used to inform clinical practice,
or referenced by the media as validated information.

Numerical Simulation Study on the Electrical Properties of Tin-based Perovskite TFT Based on Bilayer Structure

Yingtao Xie

xieyt@cqupt.edu.cn

Chongqing University of Posts and Telecommunications

Baocheng Xia

Chongqing University of Posts and Telecommunications

Yuan Zhang

Chongqing University of Posts and Telecommunications

Rui Xie

Chongqing University of Posts and Telecommunications

Xin Deng

Chongqing University of Posts and Telecommunications

Research Article

Keywords: defect density of states, threshold voltage drift, MASnI3,bilayer, thin-film transistors

Posted Date: March 18th, 2026

DOI: https://doi.org/10.21203/rs.3.rs-9127632/v1

License: This work is licensed under a Creative Commons Attribution 4.0 International License.
Read Full License

Additional Declarations: No competing interests reported.

Version of Record: A version of this preprint was published at Journal of Computational Electronics on June 20th, 2026. See the published version at https://doi.org/10.1007/s10825-026-02585-6.

Numerical Simulation Study on the Electrical Properties of Tin-based Perovskite TFT Based on Bilayer Structure

Yingtao Xie[1,3*], Baocheng Xia[2], Yuan Zhang[1], Rui Xie[1], Xin Deng[2]

[1*]Department of Electronic Engineering, Chongqing University of Posts and Telecommunications, Chongwen Road, Chongqing, 400065, Chongqing, China.

[2]Department of Integrated Circuits, Chongqing University of Posts and Telecommunications, Chongwen Road, Chongqing, 400065, Chongqing, China.

[3]Information Materials and Intelligent Sensing Laboratory of Anhui Province, Anhui University, Jiulong Road, Hefei, 230000, Anhui, China.

*Corresponding author(s). E-mail(s): xieyt@cqupt.edu.cn;
Contributing authors: summerbc@126.com; 1030804779@qq.com;
422362894@qq.com; 2814067028@qq.com;

Abstract

The methylammonium tin iodide ($MASnI_3$) thin-film transistor (TFT) still has key electrical performance problems such as threshold voltage drift and unstable mobility in practical applications. This is mainly due to the unreasonable distribution of defect density of states (DOS) caused by inherent defects in the material (such as tin vacancies). To address this deficiency, this paper proposes a novel bilayer $MASnI_3$ TFT structure, which utilizes the interlayer chemical potential difference to suppress the formation of tin vacancies, thereby optimizing the defect density distribution to improve device performance. Based on the two-dimensional device simulator of TCAD, the influence of defect DOS parameters such as tail state-donor state, Gaussian-class dependent state on the electrical characteristics of the device was systematically studied. The simulation results show that, compared with the traditional single-layer structure, the bilayer $MASnI_3$ TFT can adjust the threshold voltage to about 1 V and stabilize the saturation mobility at 11 $cm^2/V{\cdot}s$, providing a new structural optimization

scheme for solving the performance bottleneck of tin-based perovskite TFT and offering theoretical guidance for the preparation of high-performance perovskite TFT.

Keywords: defect density of states, threshold voltage drift, $MASnI_3$,bilayer, thin-film transistors

1 Introduction

Over the past decade, organic metal halide perovskite thin film transistors (TFTs) have garnered significant attention due to high carrier mobility, excellent stability, and relatively simple fabrication processes [1–3]. Specially tin-based P-type perovskite has become a critical research focus, due to their lead-free nature, superior environmental compatibility and outstanding electrical properties, with a theoretical carrier mobility of 10–100 $cm^2/V{\cdot}s$ and a bandgap of approximately 1.2–1.4 eV. However, tin-based P-type perovskite TFTs still face numerous challenges in practical applications, particularly concerning critical electrical properties such as significant threshold voltage drift and mobility instability [4–6]. These issues likely stem from the high susceptibility of Sn^{2+} to oxidation into Sn^{4+}, which generates high defect densities within the crystal structure and causes unnecessary P-type self-doping, ultimately resulting in a comprehensive deterioration of device stability [7–9]. Furthermore, the crystallization kinetics of tin-based perovskites are extremely rapid and difficult to control. This rapid crystallization often results in disordered thin films, small grain sizes, low coverage, and the generation of high-density grain boundaries and bulk defects. These defects act as non-radiative recombination centers and accelerate film degradation in water-oxygen environments [10, 11].

In the fabrication of tin-based TFTs, device stability is commonly improved by modifying component ratios or incorporating dopants such as guanidinium iodide (GAI) and resorcinol [12, 13]. Although these approaches can passivate defects and lower defect density, the physical mechanisms underlying device degradation remain unclear. Therefore, it is necessary to conduct research from the perspective of device modeling. Existing modeling studies typically focus on optimizing key device parameters, including threshold voltage and mobility, with adjusting the defect density within a conventional single-layer defect density of states (DOS) [14, 15]. However, precise control of these parameters is highly sensitive to various fabrication conditions, such as the semiconductor composition and crystallization temperature. It is difficult to achieve stable control during the film deposition and device fabrication process. In contrast, a bilayer structure offers distinct advantages [16, 17]. By modulating the thicknesses of different functional layers, the spatial distribution of hole concentration can be effectively controlled, this enables more controllable modulation of key electrical properties such as threshold voltage and mobility. This strategy benefits from lower process complexity and facilitates more consistent optimization and stabilization of device performance.

Based on this, this paper proposes a bilayer-structured $MASnI_3$ TFT. Through numerical simulation analysis, the electrical properties such as the threshold voltage are optimized to explore the potential physical mechanisms behind threshold voltage drift. First, the TACD 2D device simulator was employed to investigate the influence of density of states distributions—specifically the valence band tail density (NTD) and Gaussian-like acceptor density (NGA)—on transfer characteristics and electrical properties. Subsequently, based on these findings, a bilayer $MASnI_3$ TFT with distinct DOS distributions was constructed. The results show that the thickness of different defect layers has a significant impact on the electrical parameters such as threshold voltage, saturation mobility, and subthreshold swing. The observed threshold voltage drift in $MASnI_3$ TFTs may stem from excessively high hole concentrations introduced by the acceptor density. Consequently, this study achieved spatial control of hole concentration through a bilayer $MASnI_3$ design, resolving issues such as threshold voltage drift caused by excessively high hole concentration in single-layer structures.

2 Modeling and simulation method for the density of dtates in $MASnI_3$

The crystal structure of $MASnI_3$ belongs to a polycrystalline material, which is essentially composed of a series of grains and grain boundaries. Within the grains, the lattice arrangement is relatively regular, whereas in the grain boundary regions, the lattice arrangement appears disordered, featuring a large number of dangling bonds. These dangling bonds not only disrupt the periodic potential field, creating potential barriers, but also introduce defect energy levels within the bandgap, thereby generating trap states. The nature of these defects allows them to function as electron traps in n-type materials or as hole traps in p-type materials, explaining the observed conductivity. Multiple physical models exist for the conduction mechanism in polycrystalline channel TFTs. These models are typically based on two approaches: the effective medium approximation method and the discrete grain method, where only the boundaries are occupied by trap states. The former is applicable when grain sizes are much smaller than device dimensions, while the latter is suitable for larger grain sizes. Given the device dimensions of 500 μm $\times$ 100 μm in this study, the effective medium approximation is employed [18, 19]. $MASnI_3$ often contains abundant tin vacancies and iodine vacancies. These vacancies introduce deep-level defects, while shallow-level defects primarily result from the dynamic disorder inherent in organic-inorganic hybrid perovskites, such as the rotation of the organic cation MA^+. To accurately model devices fabricated from polycrystalline materials, a continuous density of states description is required. This involves representing the DOS as a combination of an exponential distribution for the tail states and a Gaussian distribution for the deep energy states.

Use equations (1) and (2) to calculate the effective state density in the conduction band (N_C) and the effective state density in the valence band (N_V), respectively.

$$N_c = 2\left(\frac{2\pi M_c kT}{h^2}\right)^{3/2} \tag{1}$$

$$N_V = 2\left(\frac{2\pi M_V kT}{h^2}\right)^{3/2} \tag{2}$$

Here, kT = 25 meV, and h is Planck's constant. At room temperature (300 K), the N_c and N_V values for $MASnI_3$ are both 1×10^{18} cm^{-3}/eV.

The density of states function g(E) consists of four energy bands: two tail bands (one donor-like valence band and one acceptor-like conduction band) and two deep-level energy bands modeled using Gaussian distributions (one acceptor-like and one donor-like), namely the acceptor-like conduction band tail state $g_{TA}(E)$, the donor-like valence band tail state $g_{TD}(E)$, the acceptor-like ground state density $g_{GA}(E)$, and the donor-like ground state density $g_{GD}(E)$, as shown in Figure 1.

$$g(E) = g_{TA}(E) + g_{TD}(E) + g_{GA}(E) + g_{GD}(E) \tag{3}$$

Where E is the trap energy, and the subscripts (T, G, A, D) represent tail states, Gaussian states (deep levels), acceptor-like states, and donor-like states, respectively.

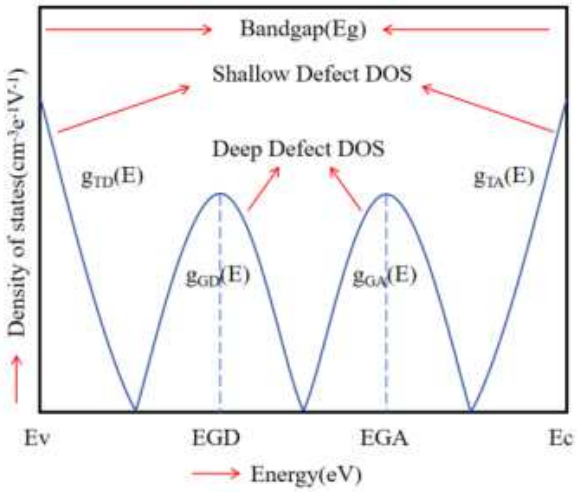


Fig. 1 DOS model for $MASnI_3$ TFT.

The acceptor-like conduction band tail states $g_{TA}(E)$ are given by Equation (4), where EC is the energy at the bottom edge of the conduction band, NTA is the intercept density at the conduction band edge when E=E_C (conduction band tail density), and WTA is the slope of the conduction band tail (characteristic decay energy of the acceptor-like tail states).

$$g_{TA}(E) = NTA \exp\left(\frac{E - E_c}{WTA}\right) \tag{4}$$

The donor-like valence band tail states $g_{TD}(E)$ are given by Equation (5), where E_V is the energy at the top edge of the valence band, NTD is the intercept density

at the valence band edge when $E = E_V$ (valence band tail density), and WTD is the slope of the valence band tail (characteristic decay energy of the donor-like tail states).

$$g_{TD}(E) = NTD \exp\left(\frac{E_V - E}{WTD}\right) \tag{5}$$

The acceptor-like density of states $g_{GA}(E)$ is given by Equation (6), where EGA is the mean energy of tin vacancies (energy corresponding to the peak of the acceptor-like Gaussian states), NGA is the peak value of tin vacancies (density of Gaussian acceptor-like states), and WGA is the standard deviation of tin vacancies (characteristic decay energy of the acceptor-like Gaussian states).

$$g_{GA}(E) = NGA \exp\left[-\left(\frac{EGA - E}{WGA}\right)^2\right] \tag{6}$$

The donor-like density of states $g_{GD}(E)$ is given by Equation (7), where EGD is the mean energy of iodine vacancies (energy corresponding to the peak of the donor-like Gaussian states), NGD is the peak value of iodine vacancies (density of Gaussian donor-like states), and WGD is the standard deviation of iodine vacancies (characteristic decay energy of the donor-like Gaussian states).

$$g_{GD}(E) = NGD \exp\left[-\left(\frac{E - EGD}{WGD}\right)^2\right] \tag{7}$$

All parameters in the numerical simulation are listed in Table 1.

3 Results and discussion

3.1 Effect of key DOS parameters on the performance of $MASnI_3$ TFT devices

For the simulation of key DOS parameters in $MASnI_3$ TFTs, a bottom-gate top-contact device structure as shown in Fig. 2(a) was employed. The channel aspect ratio (W/L) is 500 μm/100 μm. The substrate is heavily doped(n++) p-type Si with a 40 nm thick. The source (S) and drain (D) are 40 nm thick Au electrodes. The semiconductor channel layer (SC) is 40 nm thick $MASnI_3$, and the gate insulator (GI) is a 100 nm thick SiO_2. In the simulation, the work function of the Au electrodes was set to 5.1 eV, and the material parameters and density of states parameters for $MASnI_3$ are shown in Table 1. Figure 2(b) displays the Id-Vg transfer characteristic curve based on the parameters of Table 1, where Vds = -40 V and the gate voltage Vg is scanned from -40 V to 40 V. The extracted electrical parameters from the simulation data are: Vth = 2.40 V, μ_{sat} = 25.32 cm^2/Vs, SS = 0.29 V/dec. This indicates that the model and DOS parameters can effectively realize the simulation analysis of $MASnI_3$ perovskite TFTs. Simulations and analysis of major defects in $MASnI_3$ indicate that tin vacancies and iodine vacancies primarily introduce defect states characterized by NGA (gaussian-like

Table 1 Simulation Parameters of $MASnI_3$ TFTs [20, 21]

Simulation parameters	Numerical value	Units	Description
N_C	1×10^{18}	cm^{-3}/eV	Effective state density of conduction bands
N_V	1×10^{18}	cm^{-3}/eV	Effective state density of valence bands
μ_n	20	$cm^2/V{\cdot}s$	Electron band mobility
μ_p	20	$cm^2/V{\cdot}s$	Hole band mobility
NTA	5×10^{18}	cm^{-3}/eV	Conduction Band Tail State Density
NTD	5×10^{18}	cm^{-3}/eV	Valence Band Tail State Density
NGA	5×10^{15}	cm^{-3}/eV	Gaussian-like acceptor state density
NGD	5×10^{15}	cm^{-3}/eV	Gaussian-like donor state density
WTA	0.016	eV	Slope of conduction band tail
WTD	0.016	eV	Slope of valence band tail
WGA	0.09	eV	Standard deviation of acceptor-like Gaussian states
WGD	0.09	eV	Standard deviation of donor-like Gaussian states
EGA	1.28	eV	peak energy of acceptor-like Gaussian states
EGD	0.78	eV	peak energy of donor-like Gaussian states
E_g	1.3	eV	Bandgap
x_e	4.17	eV	Electron affinity
ϵ	8.2		Dielectric constant

acceptor states) and NTD (valence band tail states) [22]. Therefore, NGA and NTD are selected as the focus of this study.

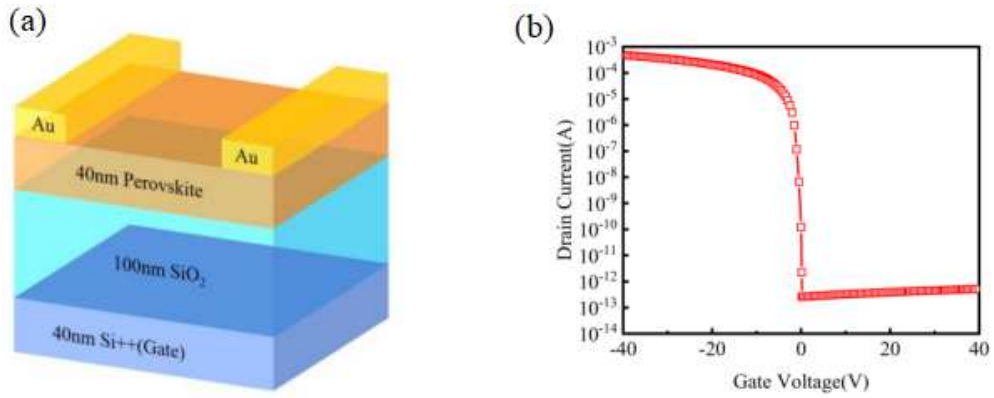


Fig. 2 (a) Two-dimensional $MASnI_3$ TFT device simulation structure. (b) Transfer characteristic curve of $MASnI_3$ TFT under Vds=-40 V.

To investigate the influence of the NTD parameter, different NTD values were set as follows: 5×10^{18} cm^{-3}/eV, 5×10^{19} cm^{-3}/eV, 5×10^{20} cm^{-3}/eV, 5×10^{21} cm^{-3}/eV, and 5×10^{22} cm^{-3}/eV. Figure 3 shows the transfer characteristic curves and the density of states distribution under different NTD values.

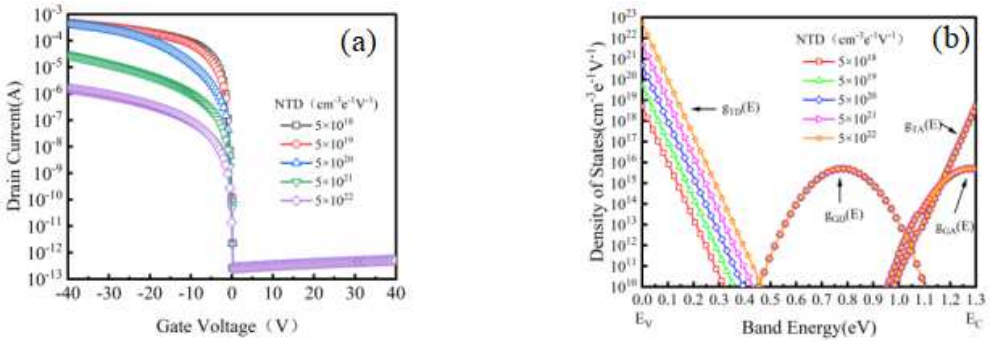


Fig. 3 (a) Transfer characteristic curves of single $MASnI_3$ TFTs under different NTD values. (b) Density of states distributions under different NTD values.

As shown in Fig. 3(a), with the increase of NTD from 5×10^{18} cm^{-3}/eV to 5×10^{22} cm^{-3}/eV, the threshold voltage (Vth) shifts negatively from –2.40 V to –10.93 V, the saturation mobility (μ_{sat}) drops from 25.32 $cm^2/V{\cdot}s$ to 0.01 $cm^2/V{\cdot}s$, and the subthreshold swing (SS) rises from 0.29 V/dec to 0.38 V/dec. These results demonstrate that NTD significantly influences both the threshold voltage and saturation mobility. Notably, once NTD exceeds 5.00×10^{19} cm^{-3}/eV, its effect on the electrical characteristics becomes markedly more pronounced. The increase in NTD causes a distinct leftward shift of the transfer characteristic curve of the $MASnI_3$ TFT, substantially altering the on-state behavior. This can be attributed to the rise in trap density near the valence band edge with increasing NTD. Under negative gate bias, the energy band bends upward, shifting the Fermi level closer to the valence band. As a result, more trap states within the bandgap become active in capturing holes, thereby reducing the population of free hole carriers. Consequently, a smaller negative gate voltage is sufficient to induce the same channel conductivity, explaining the observed negative shift in Vth.

To investigate the influence of the NGA parameter, different NGA values were set as follows: 5×10^{15} cm^{-3}/eV, 5×10^{16} cm^{-3}/eV, 5×10^{17} cm^{-3}/eV, 5×10^{18} cm^{-3}/eV, and 5×10^{19} cm^{-3}/eV. Figure 4 shows the transfer characteristic curves (semi-logarithmic coordinates) and the density of states distribution under different NGA values.

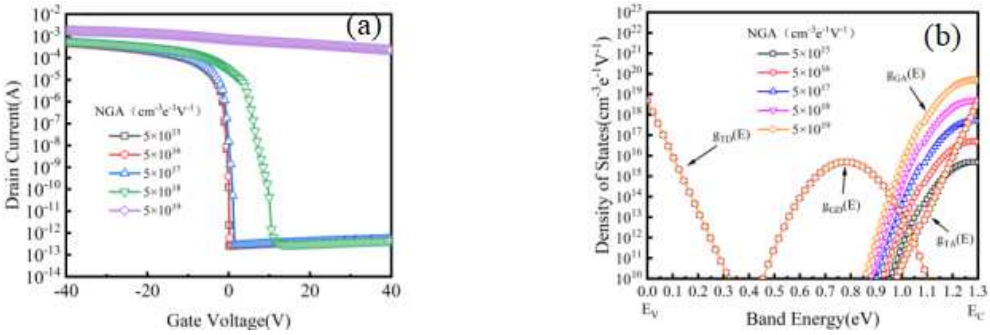


Fig. 4 (a) Transfer characteristic curves of single $MASnI_3$ TFTs under different NGA values. (b) Density of states distributions under different NGA values.

As shown in Fig. 4, when the NGA value increases sequentially from 5×10^{15} cm^{-3}/eV to 5×10^{18} cm^{-3}/eV, the threshold voltage rises from -2.40 V to 4.00 V. The saturation mobility (μ_{sat}) drops sharply to 15.07 $cm^2/V{\cdot}s$ when NGA reaches 5×10^{18} cm^{-3}/eV, while the subthreshold swing increases from 0.29 $V{\cdot}dec^{-1}$ to 7.34 $V{\cdot}dec^{-1}$. The increase in NGA causes a rightward shift in the transfer characteristic curve of the perovskite TFT. This effect becomes more pronounced when NGA reaches 5×10^{18} cm^{-3}/eV or higher. Notably, when NGA reaches 5×10^{19} cm^{-3}/eV, $MASnI_3$ loses its semiconductor properties and behaves more like a conductor. The possible reason for this is that the increase in NGA requires electrons to gain more energy for emission, meaning more electrons are trapped by acceptor-like states. As a result, the number of holes available for recombination is reduced.

3.2 Effect of Bilayer $MASnI_3$ Structures on the Electrical Performance of TFTs

Considering that the modulation of defect state density parameters in a single-layer DOS is influenced by complex factors such as thin-film composition ratios, making practical control challenging, simulations of individual DOS parameters reveal two notable phenomena: an increase in the valence band tail state density (NTD) ultimately leads to a sharp reduction in hole saturation mobility, when NTD approaches 5×10^{21} cm^{-3}/eV, the saturation mobility approaches 1 $cm^2/V{\cdot}s$; meanwhile, increasing the Gaussian-like acceptor density (NGA) causes a positive drift in the threshold voltage. This positive drift makes it more difficult to turn off the drain current in the TFT. When NGA reaches around 5×10^{19} cm^{-3}/eV, the transfer characteristic curve exhibits on-state characteristics. To address these issues, we attempted to combine the semiconductor layer $MASnI_3$ into two layers with distinct DOS and thicknesses: the NTD layer, adjacent to the back channel, has an NTD of 4×10^{21} cm^{-3}/eV, with other DOS parameters identical to those in Table 1; the NGA layer, adjacent to the front channel, has an NGA of 7×10^{18} cm^{-3}/eV, with the remaining DOS parameters identical to those in Table I. During simulations, the total semiconductor layer thickness was maintained at 40 nm, shown in Fig. 4 (a). By adjusting the thickness of the

NGA layer to 5 nm, 10 nm, 15 nm, 20 nm, 25 nm, 30 nm, and 35 nm, we investigated its impact on TFT performance. Figure 5 presents the transfer characteristic curves under varying NGA layer thicknesses, along with comparative analyses of threshold voltage and mobility.

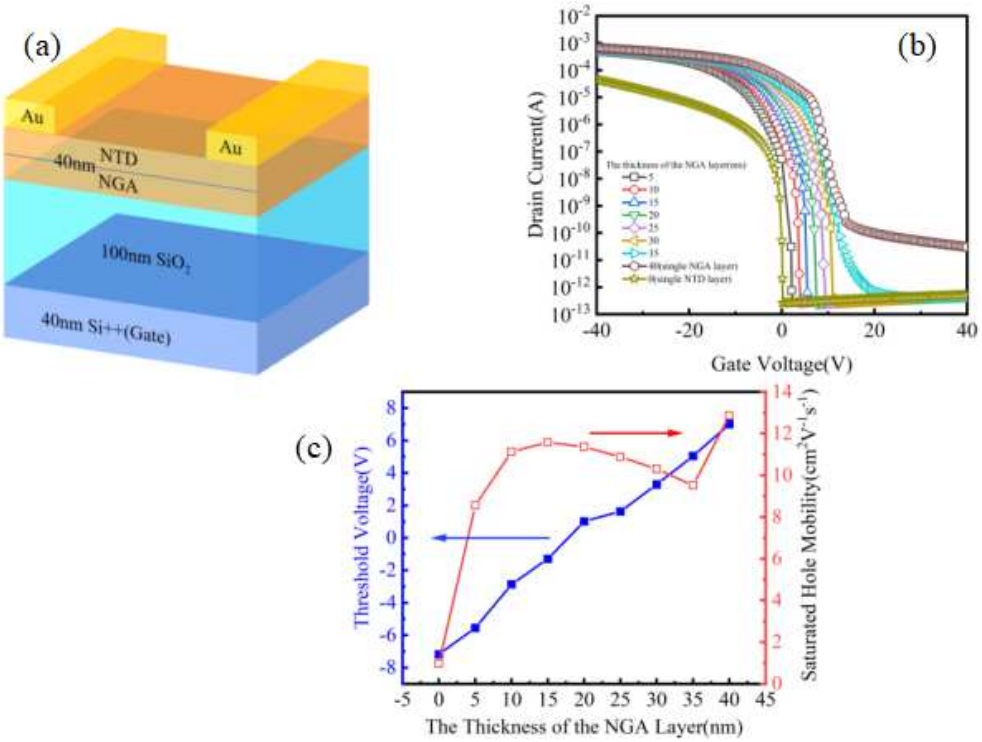


Fig. 5 (a) 40nm Bilayer $MASnI_3$ TFTs device structure with the fixed NGA and NTD values. (b) (c) Electrical characteristic curves with varying bilayer thicknesses (b) Transfer characteristic curves. (c) Threshold voltage and hole mobility.

As shown in Fig. 5, when the semiconductor layer thickness remains constant at 40 nm and the NGA layer thickness increases from 5 nm to 35 nm, the transfer characteristic curve exhibits a rightward shift, with the threshold voltage gradually increasing from -5.56 V to 5.05 V. In contrast, the threshold voltages obtained from the control group NTD=4×10^{21} cm^{-3}/eV and the control group NGA=7×10^{18} cm^{-3}/eV were -7.18 V and 7.00 V, respectively. It can be observed that in the double-layer $MASnI_3$ structure, the device threshold voltage increases linearly with increasing NGA layer thickness. Therefore, appropriately introducing a certain thickness of NTD layer on the back channel side can suppress the threshold voltage drift of the TFT. The hole saturation mobility increased from 8.56 $cm^2/V{\cdot}s$ to 11.58 $cm^2/V{\cdot}s$ before decreasing to 9.52 $cm^2/V{\cdot}s$. The hole mobility values obtained for the control group NTD=4×10^{21} cm^{-3}/eV and control group NGA=7×10^{18} cm^{-3}/eV were 0.96 $cm^2/V{\cdot}s$ and 12.86

$cm^2/V{\cdot}s$. The increase in mobility between 5-15 nm may result from elevated hole concentration. Between 15-35 nm, excessive holes intensify carrier scattering, reducing hole mobility. This is corroborated in Fig. 7, where the hole concentrations in the back channel and front channel between 15-35 nm are generally higher than those between 5-15 nm. Therefore, introducing an appropriately thick NGA layer can mitigate the issue of excessively low hole mobility. Furthermore, when an NGA layer was introduced on the front channel side in the control group (NTD=4×10^{21} cm^{-3}/eV), the on-state current of the $MASnI_3$ TFT increased by an order of magnitude. As the NGA layer thickness increased, the on-state current approached 0.001 A and remained nearly constant. This behavior may be related to electron trapping by the NGA layer.

Fig. 6 shows the channel current density distribution at Vgs = 0 V and Vds = -40 V for different NGA layer thicknesses. It can be observed that as the NGA layer thickness increases, the channel current density thickness increases from 5 nm to approximately 35 nm, with the corresponding maximum channel current density increasing by two orders of magnitude. This indicates an enhancement in the average channel current density, explaining why the increased NGA layer thickness at Vgs=0 V leads to higher drain current in Fig. 5(a). To turn off this TFT, a positive gate voltage must be applied to attract electrons to the lower half of the channel for hole recombination, thereby reducing the thickness of the channel current density distribution. This gate voltage is the TFT's threshold voltage, consistent with the changes shown in Fig. 5(b). The positive drift of the threshold voltage partially accounts for the rightward shift in the TFT transfer characteristic curve in Fig. 5(a). The increase in channel current density values with thickness in Fig. 6 leads to a rise in the TFT off-state current. Based on the approximate linear relationship between threshold voltage and NGA layer thickness shown in Fig. 5(b), when the NGA layer thickness increases to 40 nm, the off-state current is significantly enhanced. If the NGA value continues to increase beyond this point, the electrical characteristics of the $MASnI_3$ TFT exhibit properties approaching those of a conductor, which aligns with the NGA=5×10^{19} cm^{-3}/eV value in Fig. 4(a). On the other hand, simulations of different NGA layer thicknesses reveal that when the NGA layer thickness reaches 20 nm or more, the operational mode of this bilayer $MASnI_3$ TFT shifts from enhancement mode to depletion mode. This occurs because at Vgs = 0 V, the excessively high hole concentration has already formed a conductive channel. In such cases, a larger positive gate voltage is typically required to deplete the holes.

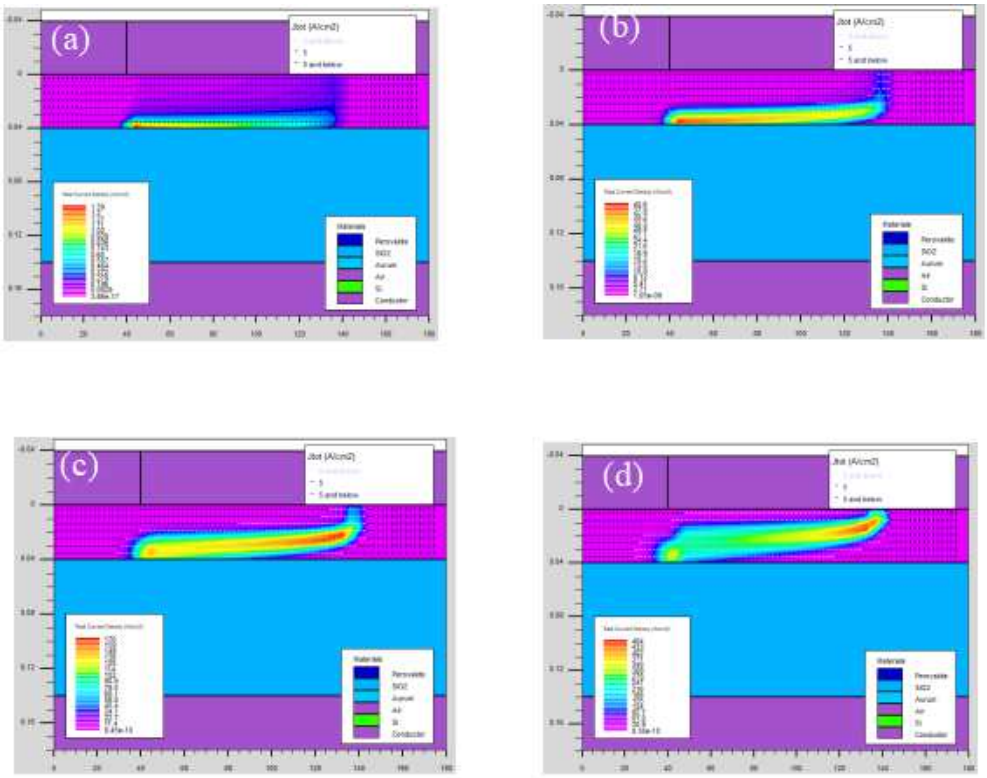


Fig. 6 Current density distribution of bilayer $MASnI_3$ TFTs under different NGA-layer thickness (a) 5 nm (b) 15 nm (c) 25 nm (d) 35 nm.

Fig. 7 shows the variation in hole concentration between the back channel and the front channel of the semiconductor layer at a gate-source voltage of 0 V for different NGA layer thicknesses. It can be observed that as the NGA layer thickness increases from 5 nm to 35 nm, the channel hole concentration increases by approximately two orders of magnitude. This indicates that the channel hole concentration can be controlled by adjusting the NGA layer thickness, thereby regulating the channel current density as shown in Fig. 6. This explains why the increase in NGA layer thickness in Fig. 5(a) leads to an increase in drain current. Simultaneously, it demonstrates that different NGA thicknesses require distinct gate voltages for depletion, meaning the threshold voltage exhibits positive drift with increasing NGA layer thickness. Therefore, controlling the NGA layer thickness can suppress threshold voltage drift, which can be achieved by overlaying an NTD layer on the NGA layer.

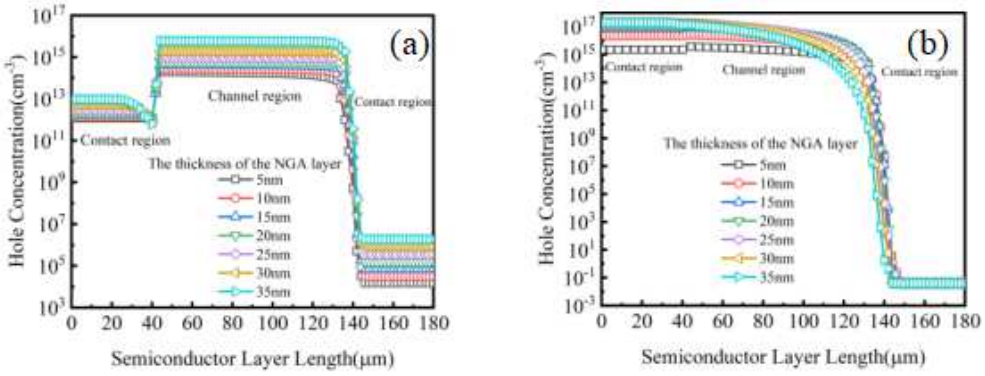


Fig. 7 Hole channel concentration of $MASnI_3$ TFTs with different NGA layer thicknesses (a) At 3 nm depth in the back channel. (b) At 3 nm depth in the front channel.

4 Conclusion

This study investigates the influence of key parameters NTD (valence band tail density) and NGA (Gaussian-like acceptor density) in the DOS on the transfer characteristic curves and electrical properties of $MASnI_3$ TFTs. Based on device characteristics obtained from simulations of these two key parameters, combined simulations of varying thicknesses for the NGA layer and NTD layer demonstrate that the bilayer $MASnI_3$ structure and simulated DOS parameters effectively explain the threshold voltage drift observed in conventional tin-based perovskite TFTs. These results provide a theoretical foundation for addressing the threshold voltage drift issues encountered in practical fabrication. In the future, we aim to further leverage density functional theory to investigate the influence of the atomic structure of $MASnI_3$ on its density of states, thereby achieving higher-stability $MASnI_3$ TFTs.

References

[1] G. Xing et al., "Long-range balanced electron-and hole-transport lengths in organic-inorganic CH3NH3PbI3," Science., vol. 342, no. 6156, pp. 344-347, Oct 2013, doi: 10.1126/science.1243167.

[2] S. D. Stranks et al., "Electron-hole diffusion lengths exceeding 1 micrometer in an organometal trihalide perovskite absorber," Science., vol. 342, no. 6156, pp. 341-344, Oct 2013, doi: 10.1126/science.1243982.

[3] Q. Dong et al., "Electron-hole diffusion lengths¿ 175 μm in solution-grown CH3NH3PbI3 single crystals," Science., vol. 347, no. 6225, pp. 967-970, Feb 2015, doi: 10.1126/science.aaa5760.

[4] F. Zhang et al., "Two-dimensional organic–inorganic hybrid perovskite field-effect transistors with polymers as bottom-gate dielectrics," Journal of Materials

Chemistry C., vol. 7, no. 14, pp. 4004-4012, Mar 2019, doi: 10.1039/C8TC06249H.

[5] J. Kim et al., "High-Performance P-Channel tin halide perovskite thin film transistor utilizing a 2D–3D Core–Shell structure," Advanced Science., vol. 9, no. 5, pp. 2104993, Dec 2022, doi: 10.1002/advs.202104993.

[6] H. Zhu et al., "High-performance and reliable lead-free layered-perovskite transistors," Advanced Materials., vol. 32, no. 31, pp. 2002717, Jun 2020, doi: 10.1002/adma.202002717.

[7] Y. Zhang et al., "Efficient tin perovskite solar cells via suppressing autoxidation in inert atmosphere," Small., vol. 20, no. 6, pp. 2306115, Sep 2024, doi: 10.1002/smll.202306115.

[8] L. Lanzetta, N. Aristidou, and S. A. Haque., "Stability of lead and tin halide perovskites: the link between defects and degradation," The Journal of Physical Chemistry Letters., vol. 11, no. 2, pp. 574-585, Jan 2020, doi: 10.10^{21}/acs.jpclett.9b02191.

[9] S. Hu et al., "Accessing Metal-Containing species in Tin–Lead perovskite precursor solutions via molecular strategies guided by the Hard–Soft Acid–Base principle," Angewandte Chemie., vol. 137, no. 41, pp. e202514010, Oct 2025, doi: 10.1002/ange.202514010.

[10] H. Cheng et al., "Understanding and minimizing non-radiative recombination losses in perovskite light-emitting diodes," Journal of Materials Chemistry C., vol. 10, no. 37, pp. 13590-13610, Jan 2022, doi: 10.1039/D2TC01869A.

[11] H. Zhou et al., "Reaction-Diffusion and crystallization kinetics modulation of Two-Step deposited Tin-Based perovskite film via reducing atmosphere," Angewandte Chemie., vol. 137, no. 12, pp. e202422217, Dec 2025, doi: 10.1002/anie.202422217.

[12] K. Cao et al., "Ionic compensation for defect reduction and enhanced performance of tin-based perovskite solar cells," Journal of Power Sources., vol. 558, pp. 232595, Feb 2023, doi: 10.10^{16}/j.jpowsour.2022.232595.

[13] Q. Wang et al., "Towards highly stable Sn^{2+} electrolyte for aqueous tin batteries using hydroquinone antioxidant," Angewandte Chemie International Edition., vol. 64, no. 7, pp. e202418928, Jan 2025, doi: 10.1002/anie.202418928.

[14] D. Shamalia and N. Tessler., "Device simulations of perovskite transistors containing mobile ions and their relevance to experimental data," Journal of Applied Physics., vol. 135, no. 6, pp. 065501, Feb 2024, doi: 10.1063/5.0195682.

[15] C. Liu et al., "How materials and device factors determine the performance: A unified solution for transistors with nontrivial gates and transistor–diode

hybrid integration," Advanced Science., vol. 9, no. 5, pp. 2104896, Feb 2022, doi: 10.1002/advs.202104896.

[16] C. P. T. Nguyen et al., "Enhanced electrical properties of oxide semiconductor thin-film transistors with high conductivity thin layer insertion for the channel region," Applied Surface Science., vol. 396, pp. 1472-1477, Feb 2017, doi: 10.10^{16}/j.apsusc.2016.11.194.

[17] Z. Gong et al., "Solution processed thin-film transistors with bilayer channel consisting of ZnO nanoparticles and SnO2," Optical Materials., vol. 128, pp. 112401, Jun 2022, doi: 10.10^{16}/j.optmat.2022.112401.

[18] W. Yan et al., "Determination of complex optical constants and photovoltaic device design of all-inorganic CsPbBr3 perovskite thin films," Optics express., vol. 28, no. 10, pp. 15706-15717, May 2020, doi: 10.1364/OE.392246.

[19] H. Babaei et al., "Observation of reduced thermal conductivity in a metal-organic framework due to the presence of adsorbates," Nature communications., vol. 11, no. 1, pp. 4010, Aug 2020, doi: 10.1038/s41467-020-17822-0.

[20] C. Pathak and S. K. Pandey., "Design, performance, and defect density analysis of efficient eco-friendly perovskite solar cell," IEEE Transactions on Electron Devices., vol. 67, no. 7, pp. 2837-2843, Jun 2020, doi: 10.1109/TED.2020.2996570.

[21] S. Kashyap, R. Pandey and J. Madan., "Simulated bending test analysis of 23

[22] K. Rajshekar and D. Kannadassan., "P-Type Cu2O thin film transistors for active matrix displays: Physical modeling and numerical simulation," IEEE Access., vol. 9, pp. 158842-158851, Nov 2021, doi: 10.1109/ACCESS.2021.3130999.